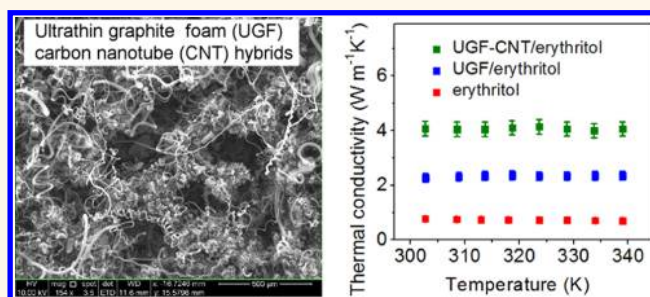


Continuous Carbon Nanotube—Ultrathin Graphite Hybrid Foams for Increased Thermal Conductivity and Suppressed Subcooling in Composite Phase Change Materials

Iskandar Kholmanov,^{*,†,‡} Jaehyun Kim,[†] Eric Ou,[†] Rodney S. Ruoff,^{§,⊥} and Li Shi^{*,†}

[†]Texas Materials Institute and Department of Mechanical Engineering, The University of Texas at Austin, Austin, Texas 78712, United States, [‡]CNR-INO, Sensor Lab, The University of Brescia, Via Branze 45, 25123, Brescia, Italy, [§]Center for Multidimensional Carbon Materials, Institute for Basic Science (IBS), Ulsan 689-798, Republic of Korea, and [⊥]Department of Chemistry, Ulsan National Institute of Science and Technology (UNIST), Ulsan 689-798, Republic of Korea

ABSTRACT Continuous ultrathin graphite foams (UGFs) have been actively researched recently to obtain composite materials with increased thermal conductivities. However, the large pore size of these graphitic foams has resulted in large thermal resistance values for heat conduction from inside the pore to the high thermal conductivity graphitic struts. Here, we demonstrate that the effective thermal conductivity of these UGF composites can be increased further by growing long CNT networks directly from the graphite struts of UGFs into the pore space. When erythritol, a phase change material for thermal energy storage, is used to fill the pores of UGF—CNT hybrids, the thermal conductivity of the UGF—CNT/erythritol composite was found to increase by as much as a factor of 1.8 compared to that of a UGF/erythritol composite, whereas breaking the UGF—CNT bonding in the hybrid composite resulted in a drop in the effective room-temperature thermal conductivity from about $4.1 \pm 0.3 \text{ W m}^{-1} \text{ K}^{-1}$ to about $2.9 \pm 0.2 \text{ W m}^{-1} \text{ K}^{-1}$ for the same UGF and CNT loadings of about 1.8 and 0.8 wt %, respectively. Moreover, we discovered that the hybrid structure strongly suppresses subcooling of erythritol due to the heterogeneous nucleation of erythritol at interfaces with the graphitic structures.



KEYWORDS: ultrathin graphite foam · carbon nanotubes · phase change materials · composites · thermal conductivity

One of the appealing properties of individual carbon nanotubes (CNTs) and graphene sheets is their high intrinsic thermal conductivities (κ).^{1–3} In these graphitic materials phonons are the dominant heat carriers, and the intrinsic heat conduction is limited by the crystal lattice anharmonicity described by phonon–phonon umklapp scattering.⁴ However, incorporation of these individual nanostructures with substrates or other functional materials for practical applications introduces other mechanisms of phonon scattering.^{5,6} In composites with dispersed high- κ graphitic fillers for thermal management applications, phonon scattering at interfaces and boundaries is the dominant factor limiting the effective thermal conductivity.^{7,8} The interfacial

thermal resistance bottleneck can be pronounced even when the fillers form a percolated network, because of weak van der Waals bonding between the fillers. The filler structures can be engineered to increase the effective thermal conductivity. For example, aligned CNT/polymer and aligned multilayer graphene/epoxy composites have relatively high thermal conductivity compared to the corresponding composites with unaligned CNTs and multilayer graphene sheets.^{9,10} A substantial increase in the thermal conductivity of composites with hybrid nanographite–CNT fillers, in which the percolation of the dispersed graphite nanoplatelets was achieved by bridging them with CNTs, has also been reported.¹¹ Although this approach is promising, the

* Address correspondence to lishi@mail.utexas.edu (L. Shi) or iskandar.kholmanov@austin.utexas.edu (I. Kholmanov).

Received for review May 13, 2015 and accepted November 3, 2015.

Published online November 03, 2015 10.1021/acsnano.5b02917

© 2015 American Chemical Society

effective heat conduction in these composites is still limited by the random contact geometry and weak van der Waals bonding between graphite and CNTs, which results in large contact thermal resistance at junctions between the graphitic fillers.^{12,13} Hence, a 3D covalently bonded CNT–graphene structure has been proposed as a different method for reducing the junction thermal resistance and achieving isotropic thermal transport properties.¹⁴

Recently, three-dimensional (3D) interconnected ultrathin graphite foams (UGFs) have been used as high- κ fillers to overcome the thermal interface resistance problem.^{15,16} Integration of UGFs with phase change materials (PCMs), which are capable of storing and releasing a large amount of thermal energy during the solid-to-liquid and liquid-to-solid phase changes, respectively, and are suitable for a wide range of thermal management and thermal energy storage applications,^{17–19} yielded composites with considerably increased thermal conductivities.¹⁶ The rigid matrix of UGFs provides stable continuous pathways for phonon transport and maintains the high cycling stability of the PCMs. The high porosity with an ordered 3D structure and large pore sizes allow straightforward integration of UGFs with other functional materials to produce composites. However, in such composites with UGFs of a pore size as large as about 500 μm , there is still large thermal resistance for heat transfer from the low- κ PCM inside the still large pore to the high- κ UGF strut walls. Essentially, the surface to volume ratio of the existing UGF structure is much lower than that of percolated networks of graphene platelets. Therefore, new approaches to engineering the pore structure are needed to reduce the thermal resistance inside the pores, so that UGFs can maintain the desired high surface to volume ratio of graphene fillers while minimizing the internal interface thermal resistance.

Here we report an approach to modify the structure of large-pore UGFs by forming a network of CNTs inside the pores. The CNTs are directly grown on the UGF foam struts, so that the CNT networks act as high surface-to-volume ratio heat transfer fins between the foam skeletal structure and the inner spaces of the pores. Erythritol, a PCM, is impregnated into the 3D UGF–CNT hybrid structure to yield composite PCMs for thermal energy storage. Our studies demonstrate that the CNT networks grown from the UGF strut result in a further increase of the thermal conductivity of the composite PCMs compared to CNTs randomly dispersed inside the pore space, with a negligible impact of the heat of melting because of the small volume fraction occupied by the hybrid structures. Besides this conceptual advance of maximizing the surface to volume ratio of continuous graphitic fillers, we discover that the hybrid structure considerably suppresses subcooling, a common problem that causes a much lower crystallization temperature than the

melting temperature of many PCMs. Our experiments further show the suppressed subcooling is caused by heterogeneous nucleation of the PCM on the graphitic surfaces.

RESULTS AND DISCUSSION

UGFs were fabricated using a Ni template-assisted chemical vapor deposition (CVD) method, as described in the Methods section and in a prior report.¹⁵ The Ni template was then electrochemically etched away. For the as-obtained UGFs shown in Figure 1a, the average density is $0.022 \pm 0.002 \text{ g/cm}^3$, which is $\sim 1\%$ of that of highly oriented pyrolytic graphite (2.26 g/cm^3).

The conventional metal-catalyst CVD technique used to grow CNTs on oxide surfaces cannot be used to grow nanotubes on the basal plane of graphitic surfaces. For example, Fe catalysts can be deposited on the graphite surface with a wet-chemistry deposition method based on dipping the oxygen-plasma-treated UGF into an aqueous solution of $\text{Fe}(\text{NO}_3)_3$, gas phase deposition using ferrocene, or e-beam deposition of an Fe catalytic film. Due to the weak interaction with the graphitic surfaces, the metal catalysts can diffuse or evaporate at the high temperatures required for CVD reaction.^{20,21} Consequently, the obtained CNTs were usually sparse, very nonuniform over the UGF struts, and only several micrometers long and contained amorphous carbon. In this work, CNTs were grown on the UGF struts using a water-assisted catalytic CVD method.^{22,23} In this growth method, discussed in the Methods section, 1–3 nm thick Fe catalytic films were deposited on both sides of the UGF using e-beam evaporation, followed by the deposition of a 10 nm Al_2O_3 buffer layer onto the UGF–Fe surfaces by atomic layer deposition (Figure 1b). The obtained UGF–Fe– Al_2O_3 samples were placed in a quartz tube in a CVD furnace, and CNTs were grown at 750 $^\circ\text{C}$ and

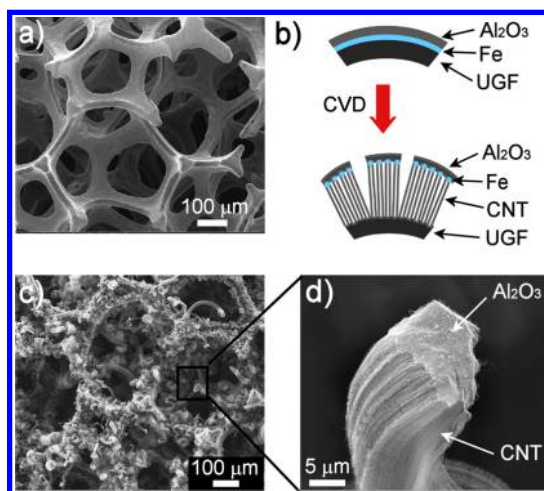


Figure 1. (a) SEM image of neat UGF. (b) Schematic of CNT growth on the UGF. (c) SEM image of the UGF–CNT hybrid structure. (d) Higher magnification SEM image of the tip of an individual CNT bundle covered by an Al_2O_3 layer.

atmospheric pressure using argon (Ar) and hydrogen (H_2) as carrier gases and acetylene (C_2H_2) as the carbon source. In this approach, the Fe catalysts were localized on the UGF surfaces by the Al_2O_3 buffer layer, and CNTs were grown by the “odako” mechanism.^{24,25} During the CVD growth process cracks in the Al_2O_3 buffer layer provided access for hydrocarbon gas to diffuse underneath the catalytic layer. CNTs thus grew directly on the UGF struts, and the Fe– Al_2O_3 layer remaining on top of the CNT bundles was lifted up by the growing nanotubes. This configuration yielded CNTs with tips attached to the floating Fe– Al_2O_3 layer and with bases directly bonded to the fixed rigid UGF struts, as illustrated in Figure 1b. With increasing length the CNT bundles form complex curved shapes (Figure 1c). Figure 1d shows a tip of an individual CNT bundle with the Al_2O_3 buffer layer on top. The length of the carbon nanotubes can be manipulated by the thickness of the Fe catalytic film (see Supporting Information, Figures S1 and S2). Fe films of 1–2 nm thickness yielded CNTs with lengths of up to 200–250 μm . These nanotubes can fully cover the surface of UGF struts, but cannot cross the pores of UGFs (Figure 1c). In order to grow longer nanotubes, we deposited 3 nm thick Fe films while keeping all other CVD parameters unchanged. This resulted in the growth of CNTs aligned in bundles with lengths from several hundreds of micrometers up to 1 mm (Figure 2a and inset). The weight of the UGF with long CNTs reaches up to 1.7–1.9 times that of the pure UGF structures.

The CNTs detached from the struts of the UGF were characterized using Raman spectroscopy (WITEC Alpha300, 532 nm wavelength, 50 \times objective; Figure 2b). The high-intensity G band centered at 1580 cm^{-1} is the first-order Raman peak representing

the sp^2 atomic arrangement of carbon atoms and is relevant to the degree of crystallinity of the nanotubes. The D band ($\sim 1350 \text{ cm}^{-1}$) is induced by disorder in a double resonance process and is indicative of defects in the sample. Another feature of the Raman spectrum is the intense G' band at 2707 cm^{-1} , which is the second-order double resonance Raman mode induced by scattering in a two-phonon process in CNTs.^{26–28} The intensity ratios between the three Raman peaks, $I(\text{G})/I(\text{D}) \approx 2.1$, $I(\text{D})/I(\text{G}') \approx 1.1$, and $I(\text{G})/I(\text{G}') \approx 2.4$, are typical for CVD-grown multiwall CNTs (MWCNTs).²⁸

The transmission electron microscopy (TEM) image (Figure 2c) shows that most of the nanotubes are multiwall with 5–10 layers and with diameters in the range 7–12 nm. The concentric rings labeled by the white rectangle in Figure 2d show the UGF–CNT interface and open-ended CNT bases or roots after they have been detached from the struts of the UGF. The observed base structure is consistent with the “odako” growth mechanism, in which metal catalysts dissolve the carbon in the topmost graphene layers of graphitic structures to initiate the CNT growth, and then further growth of nanotubes occurs due to the hydrocarbon gas.^{24,25} This mechanism yielded CNTs with bases directly bonded to the topmost graphene layers of the UGF struts.^{23,24}

Although the length of the CNT bundles in the as-prepared samples is comparable to or longer than the UGF pore size, the CNT bundles do not merge with each other and do not form interconnected networks inside the pores. To merge the CNT bundles, we immersed the samples in ethanol for 2 min at ambient conditions. When so immersed, the CNT bundles with complex curved and spiral-shaped structures were straightened and mixed with each other to form meshes inside the pores. After removing from ethanol the samples were dried at 70 $^\circ\text{C}$ for 10 min under ambient atmosphere. Due to the effects of surface tension, the evaporation of ethanol results in densification of the merged bundles,²⁹ forming CNT networks inside the pores (Figure 3a). It is worth noting that the lengths of the CNT bundles are not homogeneous. Long CNT bundles can form threads through the center of the UGF pores, while shorter ones can merge with the threads, forming percolated web-like interconnections in the pores (Figure 3b). In the intermixed bundles, the individual CNT bundles are no longer distinguishable. Only the top parts of the bundles with a rigid Fe/ Al_2O_3 floating layer are likely the CNTs grown together away from the UGF strut (Figure 3c). Ethanol treatment of UGF–CNT hybrids for which the maximum lengths of the CNT bundles are shorter than the radius of pores results in bundles attached to the UGF struts with no interconnected networks inside the pores (see Supporting Information, Figure S3). The structural changes induced by the ethanol treatment of hybrid UGF–CNT structures with long CNTs

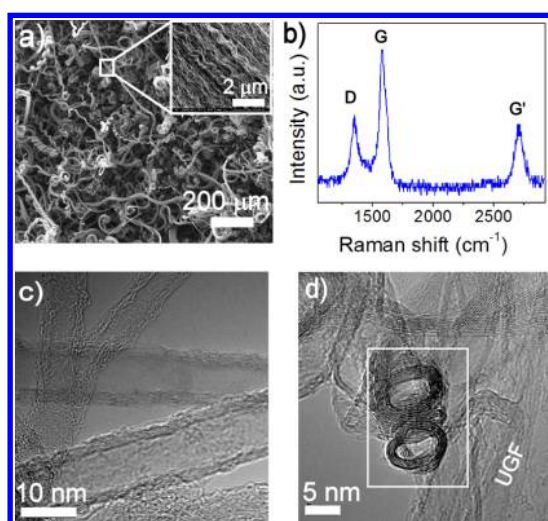


Figure 2. (a) SEM images of a UGF–CNT hybrid structure. The inset shows a high-magnification SEM image of aligned CNTs in the bundle. (b) Raman spectrum of CNTs. (c) HRTEM image of MWNTs. (d) HRTEM image of open-ended CNTs (in the white rectangle) detached from the UGF struts.

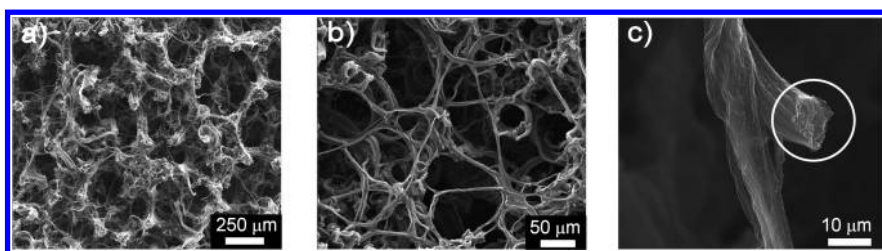


Figure 3. SEM images of UGF–CNT hybrid structure after treatment with ethanol. (a) CNTs with a length exceeding the UGF pore size; (b) CNT networks formed inside the UGF pore; (c) CNT bundle tip with an Fe/Al₂O₃ layer (indicated by the white circle) merged with another bundle inside the UGF pore.

play an important role in the effective thermal conductivity of the composites where the hybrid structures are used as thermal fillers (see below and Supporting Information).

A CNT bundle was separated from the interwoven network grown on the UGF sample and transferred to a suspended device for a four-probe thermal transport measurement of the intrinsic thermal conductance and thermal contact resistance of the bundle.³⁰ Based on the average height and lateral size of the bundle measured with atomic force microscopy (AFM), the effective thermal conductivity of the bundle is $19 \pm 2 \text{ W m}^{-1} \text{ K}^{-1}$ near room temperature (see Supporting Information, Figures S4–S6). In addition, we used an AFM cantilever resonator to measure the mass of the CNT bundle. By ignoring the presence of solvent residue and the Al₂O₃ cap in the bundle and attributing all the measured mass to the CNTs, we determined an upper limit to the average solid cross section occupied by the CNT according to the length of the bundle and the mass density of graphite. This upper limit is used to obtain a lower limit of the solid thermal conductivity of $43 \pm 2 \text{ W m}^{-1} \text{ K}^{-1}$ near room temperature. This value is about twice the effective thermal conductivity due to the high porosity of the CNT bundle (see the Supporting Information). Nevertheless, there should be room to further improve the solid thermal conductivity of the individual CNTs grown at a relatively low growth temperature of 750 °C.

It was demonstrated in a recent report that the UGFs impregnated with PCMs yielded composites with increased thermal conductivities.¹⁶ The thermal resistance of the PCM with thermal conductivity κ_p inside a single pore is on the order of $(R_1^{-1} - R_2^{-1})/4\pi\kappa_p$ between the UGF strut and the phase change front with radii R_2 and R_1 , respectively. In comparison, the thermal resistance between the UGF strut wall of a single pore and a planar heat exchanger surface located a distance R_3 away from the pore is on the order of $(R_2^{-1} - (2R_3)^{-1})/4\pi\kappa$,³¹ where κ is the effective thermal conductivity of the UGF–PCM composite. Growing nanotubes from the UGF strut wall into the pore space serves to increase both the effective κ and κ_p , with a large enhancement factor expected for κ_p because κ_p is smaller than κ without the nanotubes.

To examine the actual effects of the CNT networks, we loaded erythritol into the UGF–CNT and investigated the thermophysical properties of the obtained composite in comparison with pure erythritol and UGF/erythritol composites. Erythritol, a PCM, is a sugar alcohol with a melting point of about 119 °C and enthalpy of fusion (ΔH) of about 340 J/g, which makes it attractive for thermal energy storage applications. However, the low thermal conductivity of erythritol, about $\sim 0.78 \text{ W m}^{-1} \text{ K}^{-1}$, limits the heat charging and discharging rate into the PCM. In our experiments, erythritol (C₄H₁₀O₄, molar mass of 122.12 g/mol, from Acros Organics, 99% purity) was melted under normal atmosphere and loaded into the UGF (density of $0.022 \pm 0.002 \text{ g/cm}^3$) and UGF–CNT (density of $0.033 \pm 0.002 \text{ g/cm}^3$) matrix (see Methods section). The obtained UGF/erythritol (Figure 4a) and UGF–CNT/erythritol (Figure 4b) composites contain $98.2 \pm 0.15 \text{ wt } \%$ or $87.7 \pm 1.1 \text{ vol } \%$ and $97.1 \pm 0.15 \text{ wt } \%$ or $84.2 \pm 1.1 \text{ vol } \%$ erythritol, respectively. The results suggest the presence of void space, about 12.3 and 15.8 vol %, for UGF/erythritol and UGF–CNT/erythritol composites, respectively. These voids can be partly attributed to thermal contraction during the solidification of erythritol.

Figure 4c shows the heat capacity (C_p) of pure erythritol and the composites measured using differential scanning calorimetry (DSC, Netzsch DSC-404 F1 Pegasus). For pure erythritol we measured the heat capacity at around 302 K as $1.2 \pm 0.1 \text{ J g}^{-1} \text{ K}^{-1}$, which is similar to the data reported in the literature, $1.24 \text{ J g}^{-1} \text{ K}^{-1}$ at 302 K and $1.31 \text{ J g}^{-1} \text{ K}^{-1}$ at 340 K.^{32,33} The specific heat capacities of the UGF/erythritol and UGF–CNT/erythritol composites are similar to that of pure erythritol, indicating a negligible contribution by the carbon matrix to the C_p of the composites. This result can be explained by the low mass fraction of the carbon in the composite PCMs. In contrast, the presence of a carbon hybrid foam can result in substantially increased thermal diffusivity (α) of the composites, which is measured using a laser flash apparatus (Netzsch LFA457 Microflash) and shown in Figure 4d. UGF/erythritol and UGF–CNT/erythritol show about 3.5 and 6.4 times higher thermal diffusivities, respectively, than the $0.42 \pm 0.02 \text{ mm}^2/\text{s}$ value

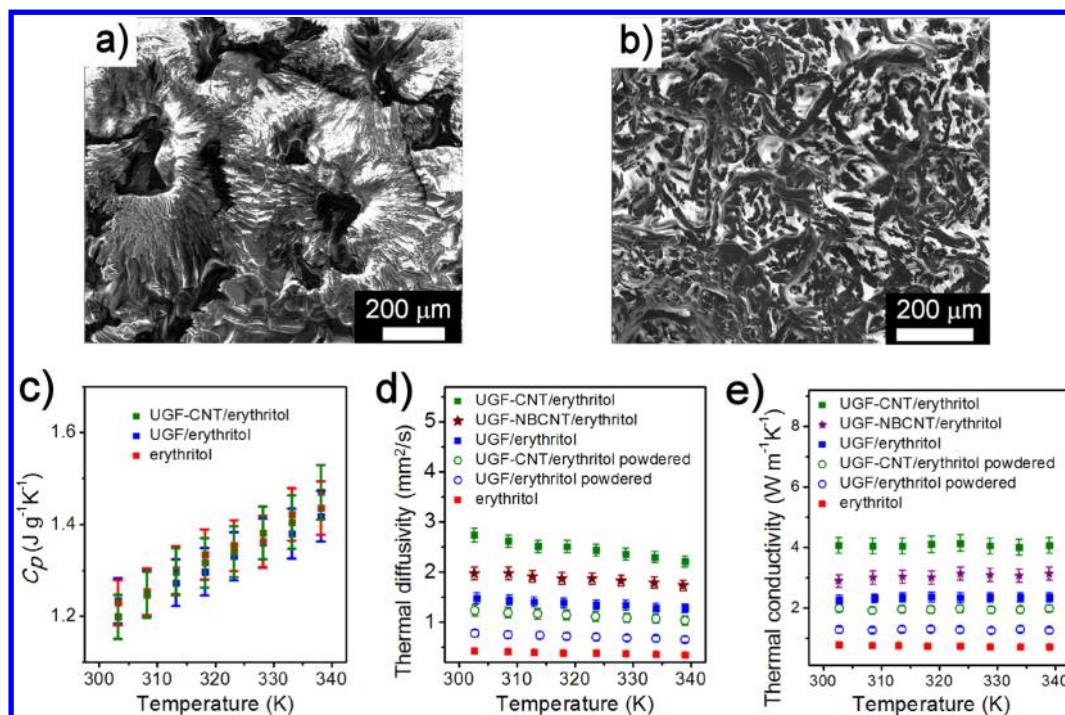


Figure 4. SEM images of (a) UGF/erythritol and (b) UGF-CNT/erythritol composites. The (c) specific heat capacity, (d) thermal diffusivity, and (e) thermal conductivity of erythritol, UGF/erythritol, and UGF-CNT/erythritol. (d) and (e) contain additional data for powdered UGF/erythritol, powdered UGF-CNT/erythritol, and UGF-NBCNT/erythritol composites. The specific heat, thermal diffusivity, and thermal conductivity data and corresponding error bars in (c), (d), and (e) are the average and random uncertainty with 95% confidence of the measurements of five samples for each type.

measured for pure erythritol at 302 K. Figure 4e shows the thermal conductivity of the samples calculated according to $\kappa = \rho \alpha C_p$, where ρ is the effective density of the samples. The thermal conductivity of pure erythritol was measured as $0.8 \pm 0.1 \text{ W m}^{-1} \text{ K}^{-1}$ at $\sim 302 \text{ K}$, which is similar to that reported in the literature: $0.733 \text{ W m}^{-1} \text{ K}^{-1}$ at 20°C .^{34,35} Similar to the thermal diffusivity curves, the thermal conductivities of UGF/erythritol ($\kappa = 2.26 \pm 0.1 \text{ W m}^{-1} \text{ K}^{-1}$) and UGF-CNT/erythritol ($\kappa = 4.09 \pm 0.3 \text{ W m}^{-1} \text{ K}^{-1}$) at 302 K are about 3 and 5.2 times higher than that of pure erythritol ($\kappa = 0.78 \pm 0.1 \text{ W m}^{-1} \text{ K}^{-1}$), respectively.

The obtained results demonstrate a substantial difference in the thermal transport properties between UGF/erythritol and UGF-CNT/erythritol composites. To gain a better understanding of the underlying mechanisms, the composites were ground into powders in which the continuous carbon structures were broken apart, as described in the Methods section. The C_p values of the ground composites show no significant difference from those of the intact composites. In contrast, α and κ of the powdered samples are considerably lower than those of the intact hybrid foam composites, as shown in Figure 4d and e.

In addition, to evaluate the role of the direct connection of CNTs to the topmost layers of UGF struts in the increased thermal conductivity of the UGF-CNT/erythritol composites, we measured the thermal conductivity of similar composites but with CNTs not directly

bonded to the UGFs. In these experiments, the CNTs were detached from CNT-UGF hybrid foams, and then these nonbounded CNTs (NBCNTs) together with erythritol were loaded into the pores of a new UGF to yield UGF-NBCNT/erythritol composites with similar CNT and UGF volume fractions to the continuous CNT-UGF hybrid foams. The thermal conductivity measurements showed that despite the similar composition, the room-temperature κ value of the UGF-NBCNT/erythritol composites is about 30% lower than that of the UGF-CNT/erythritol sample, as shown in Figure 4e. These results clearly indicate that the direct connection of CNTs with UGF results in lower thermal interface resistance between the CNTs and the UGF strut walls than that of the NBCNT-UGF junctions.

The thermal conductivity of the liquid PCM was not measured in this work because of the complication of laser flash measurements of a liquid composite sample, including the difficulty of ensuring adequate thermal contact between the liquid phase and the container because of the volume changes due to heating and phase change. Nevertheless, the thermal conductivity of liquid phase erythritol has been reported to be $0.326 \text{ W m}^{-1} \text{ K}^{-1}$ at 140°C , which is lower than the value for the solid phase, $0.78 \text{ W m}^{-1} \text{ K}^{-1}$ at $\sim 30^\circ \text{C}$.³⁴ Because of the relatively low thermal conductivity of the liquid erythritol, the enhancement factor in the effective thermal conductivity due to the UGF-CNT fillers is expected to be higher for the liquid phase PCM than for the solid phase.

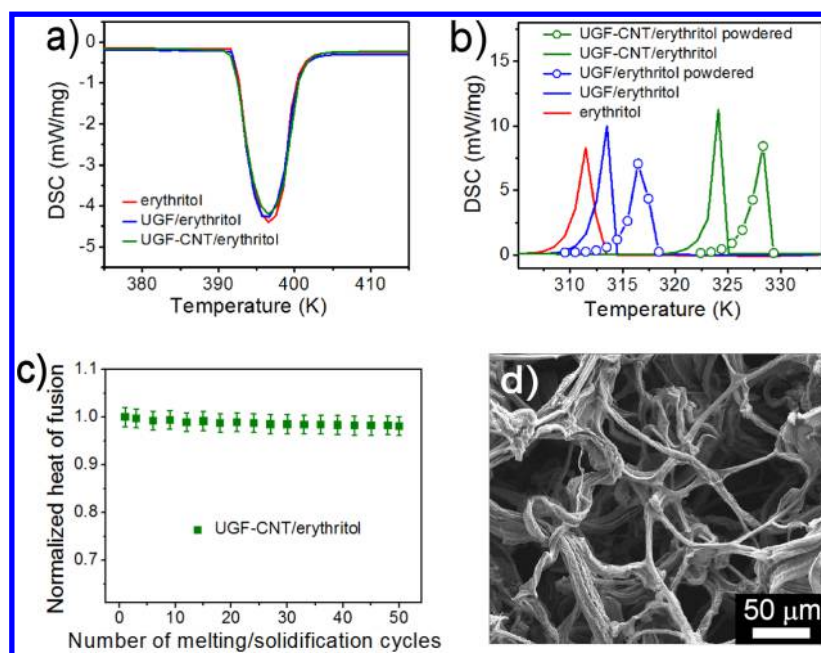


Figure 5. (a) DSC curves of melting for erythritol, UGF/erythritol, and UGF–CNT/erythritol. The heating rate is 5 K/min. (b) DSC curves of solidification for erythritol, UGF/erythritol, and UGF–CNT/erythritol and powdered UGF/erythritol and UGF–CNT/erythritol. The cooling rate was 5 K/min. The solidification temperature (T_s) was identified as the onset temperature of solidification for each sample. (c) Normalized heat of fusion as a function of the melting/solidification cycles. The data and error bars are the average and random uncertainty with 95% confidence of the measurements of five samples. (d) SEM image of the UGF–CNT filler after removing the erythritol (see text for details).

Subcooling is another critical issue that has limited the use of erythritol, many sugar alcohols, and other PCMs with relatively high heats of melting. During the subcooling process, the liquid PCM solidifies at temperatures well below the melting point because of the relatively slow nucleation process compared to the cooling rate. Subcooling occurs because a finite free energy barrier prevents formation of stable solid (spherical) nuclei with a critical radius of R_{cr} . The degree of subcooling (T_{sc}), defined as $T_{sc} = T_m - T_s$, where T_m and T_s are the onset of melting and solidification temperatures, respectively, can be expressed as $T_{sc} = (4/3)[\gamma_0 T_m / (\rho^s \Delta H R_{cr})]$,³⁶ where γ_0 is the surface free energy per unit area, ρ^s is the density of the solid, and ΔH is enthalpy of fusion. This equation indicates that the spontaneous homogeneous nucleation with stable nuclei can occur when a large T_{sc} is reached. Because the thermal energy released during solidification is used as useful energy and the solidification temperature determines the quality of the released heat, suppressing the degree of subcooling in PCMs is of great importance for latent heat energy storage.^{37,38}

To investigate the subcooling effect in UGF–CNT/erythritol composites, we measured melting and solidification curves of erythritol and the composites. Figure 5a shows no substantial difference in the melting curves of pure erythritol and the composites with $T_m = 392 \pm 0.25$ K. The latent heats of fusion of UGF/erythritol and UGF–CNT/erythritol composites are respectively only about $3.1 \pm 0.8\%$ and $5.7 \pm 0.8\%$ less than that measured for pure erythritol (332 ± 9.7 J/g)

and correspond to the weight fractions of the PCM in the composites.

The solidification temperature depends on many experimental parameters such as the cooling rate, the maximum heating temperature, and the amount of sample.³⁹ Figure 5b shows solidification curves for pure erythritol and the composites obtained using a 5 K/min cooling rate and under 50 mL/min flow of helium. For pure erythritol, we observed $T_s = 313.4 \pm 4$ K and $T_{sc} = 79 \pm 4$ K. Compared to these values, the UGF/erythritol composites show $T_s = 314.5 \pm 4$ K and a slightly reduced degree of subcooling of $T_{sc} = 78 \pm 4$ K, while in UGF–CNT/erythritol the subcooling was reduced significantly to $T_{sc} = 67 \pm 4$ K and $T_s = 325 \pm 4$ K. To understand whether the suppressed subcooling is related to the increased thermal conductivity of the hybrid foams, we measured solidification curves of the powdered composites. Despite the reduced thermal diffusivity and thermal conductivity, as shown in Figure 4e and f, the subcooling in the powdered composites is decreased further compared to the values for the intact foam composites (Figure 5b, see also Supporting Information, Table S1). This finding suggests that the suppressed subcooling is caused by heterogeneous nucleation of the sugar alcohol on the graphitic surface and benefits from the increased interface surface area in the powdered foam composites. In addition, both the surface curvature and point defect density are expected to increase considerably in both the UGF–CNT/erythritol composites and the powdered composites compared to the intact

UGF/erythritol composites. The increased interface density, curvature, and point defect density can all promote heterogeneous nucleation.^{40,41}

Based on a published report,³⁴ the density of erythritol is 1480 kg/m³ at 20 °C for the solid phase and 1300 kg/m³ at 140 °C for the liquid phase. These values correspond to a 14% increase of the volume upon melting. In comparison, the thermal expansion coefficient is negligible for graphite in this temperature range. Despite the mismatch in the thermal expansion coefficient, the composite PCMs have a high stability during the melting/solidification cycles with negligible change (<0.8%) in the values of their heat of melting after 50 cycles (Figure 5c). Figure 5d shows an SEM image of the UGF–CNT matrix after erythritol was loaded into the UGF–CNT matrix, 50 melting/solidification cycles were performed, molten erythritol was unloaded from the matrix, and the matrix was washed with DI water to remove the residual erythritol. No structural damage to the rigid matrix was observed. In addition, the figure shows that the CNTs were still attached to the UGF after the processing, indicating a strong bonding between the CNTs and the UGF struts. These results indicate that, in contrast to the types of composites with dispersed high- κ fillers that tend to aggregate, especially in liquid phases,⁴² the UGF–CNT matrix has excellent thermal, chemical, and structural stabilities under the tested conditions.

METHODS

Fabrication of UGFs. UGFs were grown on a Ni foam template (INCOFOAM, Novamet Specialty Products Corp., 42 mg/cm² foam density, average pore size of about 500 μ m and thickness of 1.5 mm) using a CVD method. The template was loaded into a 1 in. diameter quartz tube CVD furnace that was pumped to a pressure of 3×10^{-3} Torr and was then filled with a gas mixture of Ar (40 standard cubic centimeters per minute (sccm)) and H₂ (10 sccm) until reaching atmospheric pressure. The furnace was then heated to 1050 °C under a flow of this gas mixture at atmospheric pressure. The Ni foam was kept at 1050 °C under these conditions for 25 min, and then CH₄ (5 sccm) was added to the gas mixture for 1 h. Subsequently, the furnace was cooled to room temperature at a rate of 20 °C/min.

The Ni template was electrochemically etched using a 1 M aqueous solution of NiCl₂ (nickel(II) chloride hexahydrate, Sigma-Aldrich) mixed with 1 M boric acid as an electrolyte and a Ni plate as a cathode. We applied 1–4 V to obtain an initial current density of 0.5 A/cm² and kept the external field until a current density of <0.01 A/cm² was reached. The obtained UGFs were washed 8–10 times with DI water and finally rinsed in 2-propanol before drying them at 50 °C for 3 h.

Growth of CNTs. CNTs were grown by a catalytic CVD method at atmospheric pressure. Fe catalytic films were deposited on both sides of the UGF using e-beam evaporation. The relatively large pore size and small thickness (1.5 mm) of the UGF allows sufficiently uniform deposition of Fe films by this method. Consequently, CNT bundles are grown even on the inner struts of the UGF. To investigate the influence of the catalytic layer thickness, we tested Fe films with different thicknesses. A 10 nm thick Al₂O₃ buffer layer was deposited on top of the Fe film by atomic layer deposition (ALD, Cambridge NanoTech SavannahTM 200). The obtained UGF–Fe–Al₂O₃ samples were

CONCLUSIONS

We have obtained UGF–CNT hybrid materials in which the CNT bundles can form web-like networks inside the UGF pores. When integrated with erythritol, the obtained UGF–CNT/erythritol composites exhibit improved thermal conductivity and a strongly reduced degree of subcooling during the solidification of erythritol. This improved performance can be ascribed to a combination of the CNT networks directly grown on the UGF strut walls and extending into the pore space, the rigid and continuous network of the UGF itself, and the high porosity and efficient thermal transport. These characteristics together with the lightweight and relatively high corrosion resistance demonstrate the advantage of the UGF–CNT hybrid material over UGFs,¹⁶ other carbon and metal foams,^{18,43} and a wide range of dispersed carbon, metal, and oxide nanofillers.^{17,19,44} Therefore, the fabricated UGF–CNT/PCM composites represent an important advance in the active development of composites for thermal management and thermal energy storage applications. While only one end of the CNTs is directly bonded to the UGF strut wall for the hybrid structure presented here, hybrid UGF–CNT structures with both ends of the CNTs directly bonded to the UGF strut walls are expected to yield further improved thermal properties and present a promising direction for future research.

placed into the quartz tube of a CVD furnace, and the temperature of the system was increased from room temperature to 750 °C at a rate of 15 °C/min under an atmospheric pressure of a mixture of flowing argon (Ar, 500 sccm) and hydrogen (400 sccm). At 750 °C the sample was exposed to the acetylene (C₂H₂, 10 sccm) for 15 min. Additional argon gas (10 sccm) was used to carry water vapor through a bubbler into the CVD furnace to prevent the deposition of amorphous carbon. After the growth process the system was cooled to room temperature at a cooling rate of 20 °C/min.

To investigate the influence of the catalytic layer thickness, we tested three different thicknesses (1, 2, and 3 nm) of the Fe films. With the use of the CVD parameters described above, 1 and 2 nm thick Fe films yielded short CNTs (Figure S1a and b), while 3 nm thick Fe films were found to be of a sufficient thickness to obtain CNTs with lengths greater than the UGF pore diameters, as shown in Figure S1c.

Fabrication of Composite PCMs. To obtain a high filling fraction, the UGFs were treated with oxygen plasma (Plasma Preen II, Kurt J. Lesker) for 40 s in oxygen at a pressure of 1 Torr. The UGF–CNT hybrids were exposed to the same oxygen plasma for only 5 s. Erythritol was loaded into the plasma-treated carbon hybrids by slowly immersing them into molten erythritol at 130 °C, and the obtained composites were cooled to room temperature. The ground composites were prepared using an agate mortar and pestle to obtain powders with particle sizes of <50 μ m and then resolidified by melting–cooling processes for further thermal characterization tests.

PCM Thermal Property Measurements. The thermal properties of PCM and composite PCMs were measured using differential scanning calorimetry (DSC) and laser flash analysis (LFA). The amounts of the samples analyzed for melting, solidification, and heat capacity measurements were in the range 9.70–10.25 mg. The samples were placed in a standard alumina DSC pan/lid and

subjected to melting–solidification cycles under a constant helium gas flow of 50 mL/min with identical heating and cooling rates of 5 K/min in the temperature range 273–433 K. Heat capacity measurements were conducted under the same conditions in the temperature range 303–340 K. A controlled flow of liquid nitrogen was applied during cooling in order to accurately maintain a 5 K/min cooling rate. Thermal diffusivity measurements were conducted using an LFA under a constant helium gas flow of 50 mL/min in the temperature range 303–340 K with 5 K steps. The thicknesses of the samples were in the range 1.2–1.7 mm.

Conflict of Interest: The authors declare no competing financial interest.

Acknowledgment. We thank Dr. R. Piner for atomic force microscopy imaging of the nanotube bundle, G. Coloyan for her help in transferring nanotube bundle samples, and Prof. Peter Throver for helpful discussions. This work was primarily supported by the ARPA-E HEATs program (Contract No. DE-AR0000178). J.H.K. and E.O. were supported by the Office of Naval Research (Grant No. N00014-14-1-0258) and Department of Energy Office of Basic Science (Grant No. DE-FG02-07ER46377), respectively. R.S.R. was supported by IBS-R019-D1.

Supporting Information Available: The Supporting Information is available free of charge on the ACS Publications website at DOI: 10.1021/acsnano.5b02917.

Figures showing UGF–CNT samples with different CNT lengths, cross sectional view of UGF–CNT samples, and SEM images of UGF–CNT samples before and after ethanol treatment and details of thermal conductivity measurements of a CNT bundle (PDF)

REFERENCES AND NOTES

- Kim, P.; Shi, L.; Majumdar, A.; McEuen, A. P. Thermal Transport Measurements of Individual Multiwalled Nanotubes. *Phys. Rev. Lett.* **2001**, *87*, 215502.
- Marconnet, A. M.; Panzer, M. A.; Goodson, K. E. Thermal Conduction Phenomena in Carbon Nanotubes and Related nanostructured materials. *Rev. Mod. Phys.* **2013**, *85*, 1295–1326.
- Balandin, A. A. Thermal Properties of Graphene and Nanostructured Carbon Materials. *Nat. Mater.* **2011**, *10*, 569–581.
- Klemens, P. G. Theory of the A-Plane Thermal Conductivity of Graphite. *J. Wide Bandgap Mater.* **2000**, *7*, 332–339.
- Seol, J. H.; Jo, I.; Moore, A. L.; Lindsay, L.; Aitken, Z. H.; Pettes, M. T.; Li, X.; Yao, Z.; Huang, R.; Broido, D.; et al. Two-Dimensional Phonon Transport in Supported Graphene. *Science* **2010**, *328*, 213–216.
- Wang, Y.; Vallabhaneni, A. K.; Qiu, B.; Ruan, X. Two-Dimensional Thermal Transport in Graphene: A Review of Numerical Modeling Studies. *Nanoscale Microscale Thermophys. Eng.* **2014**, *18*, 155–182.
- Han, Z.; Fina, A. Thermal Conductivity of Carbon Nanotubes and Their Polymer Nanocomposites: A Review. *Prog. Polym. Sci.* **2011**, *36*, 914–944.
- Shenogina, N.; Shenogin, S.; Xue, L.; Keblinski, P. On the Lack of Thermal Percolation in Carbon Nanotube Composites. *Appl. Phys. Lett.* **2005**, *87*, 133106.
- Marconnet, A. M.; Yamamoto, N.; Panzer, M. A.; Wardle, B. L.; Goodson, K. E. Thermal Conduction in Aligned Carbon Nanotube-Polymer Nanocomposites with High Packing Density. *ACS Nano* **2011**, *5* (5), 4818.
- Li, Q.; Guo, Y.; Li, W.; Qiu, S.; Zhu, C.; Wei, X.; Chen, M.; Liu, C.; Liao, S.; Gong, Y.; et al. Ultrahigh Thermal Conductivity of Assembled Aligned Multilayer Graphene/Epoxy Composite. *Chem. Mater.* **2014**, *26*, 4459–4465.
- Yu, A.; Ramesh, P.; Sun, X.; Bekyarova, E.; Itkis, M. E.; Haddon, R. C. Enhanced Thermal Conductivity in a Hybrid Graphite Nanoplatelet – Carbon Nanotube Filler for Epoxy Composites. *Adv. Mater.* **2008**, *20*, 4740–4744.
- Estrada, D.; Pop, E. Imaging Dissipation and Hot Spots in Carbon Nanotube Network Transistors. *Appl. Phys. Lett.* **2011**, *98*, 073102.
- Yang, J.; Shen, M.; Yang, Y.; Evans, W. J.; Wei, Z.; Chen, W.; Zinn, A. A.; Chen, Y.; Prasher, R.; Xu, T. T.; Keblinski, P.; Li, D. Phonon Transport through Point Contacts between Graphitic Nanomaterials. *Phys. Rev. Lett.* **2014**, *112*, 205901.
- Varshney, V.; Patnaik, S. S.; Roy, A. K.; Froudakis, G.; Farmer, B. L. Modeling of Thermal Transport in Pillared-Graphene Architectures. *ACS Nano* **2010**, *4*, 1153–1161.
- Pettes, M. T.; Ji, H. X.; Ruoff, R. S.; Shi, L. Thermal Transport in Three-Dimensional Foam Architectures of Few-Layer Graphene and Ultrathin Graphite. *Nano Lett.* **2012**, *12*, 2959–2964.
- Ji, H.; Sellan, D. P.; Pettes, M. T.; Kong, X.; Ji, J.; Shi, L.; Ruoff, R. S. Enhanced Thermal Conductivity of Phase Change Materials with Ultrathin-Graphite Foams for Thermal Energy Storage. *Energy Environ. Sci.* **2014**, *7*, 1185–1192.
- Farid, M. M.; Khudhair, A. M.; Razack, S. A. K.; Al-Hallaj, S. A Review on Phase Change Energy Storage: Materials and Applications. *Energy Convers. Manage.* **2004**, *45*, 1597–1615.
- Lafdi, K.; Mesalhy, O.; Shaikh, S. Experimental Study on the Influence of Foam Porosity and Pore Size on the Melting of the Phase Change Materials. *J. Appl. Phys.* **2007**, *102*, 083549.
- Yavari, F.; Fard, H. R.; Pashayi, K.; Rafiee, M. A.; Zamiri, A.; Yu, Z.; Ozisik, R.; Borca-Tasciuc, T.; Koratkar, N. Enhanced Thermal Conductivity in a Nanostructured Phase Change Composite due to Low Concentration Graphene Additives. *J. Phys. Chem. C* **2011**, *115*, 8753–8758.
- Kholmanov, I. N.; Cavaleri, E.; Cepek, C.; Gavioli, L. Catalytic Chemical Vapor Deposition of Methane on Graphite to Produce graphene Structures. *Carbon* **2010**, *48*, 1619–1625.
- Kholmanov, I. N.; Cavaleri, E.; Fanetti, M.; Cepek, C.; Gavioli, L. Growth of Curved Graphene Sheets on Graphite by Chemical Vapor Deposition. *Phys. Rev. B: Condens. Matter Mater. Phys.* **2009**, *79*, 233403.
- Hata, K.; Futaba, D. N.; Mizuno, K.; Namai, T.; Yamura, M.; Iijima, S. Water-Assisted Highly Efficient Synthesis of Impurity-Free Single-Walled Carbon Nanotubes. *Science* **2004**, *306*, 1362–1364.
- Yan, Z.; Ma, L.; Zhu, Y.; Lahiri, I.; Hahm, M. G.; Liu, Z.; Yang, S.; Xiang, C.; Lu, W.; Peng, Z.; et al. Three-Dimensional Metal Graphene Nanotube Multifunctional Hybrid Materials. *ACS Nano* **2013**, *7*, 58–64.
- Pint, C. L.; Alvarez, N. T.; Hauge, R. H. Odako Growth of Dense Arrays of Single-Walled Carbon Nanotubes Attached to Carbon Surfaces. *Nano Res.* **2009**, *2*, 526–534.
- Zhu, Y.; Li, L.; Zhang, C.; Casillas, G.; Sun, Z.; Yan, Z.; Ruan, G.; Peng, Z.; Raji, A. R. O.; Kittrell, C.; et al. A Seamless Three-Dimensional Carbon Nanotube Graphene Hybrid Material. *Nat. Commun.* **2013**, *3*, 1225.
- DiLeo, R. A.; Landi, B. J.; Raffaele, R. P. Purity Assessment of Multiwalled Carbon Nanotubes by Raman Spectroscopy. *J. Appl. Phys.* **2007**, *101*, 064307.
- Dresselhaus, M. S.; Dresselhaus, G.; Saito, R.; Jorio, A. Raman Spectroscopy of Carbon Nanotubes. *Phys. Rep.* **2005**, *409*, 47–99.
- Lehman, J. H.; Terrones, M.; Mansfield, E.; Hurst, K. E.; Meunier, V. Evaluating the Characteristics of Multiwall Carbon Nanotubes. *Carbon* **2011**, *49*, 2581–2602.
- Zhang, M.; Fang, S.; Zakhidov, A. A.; Lee, S. B.; Aliev, A. E.; Williams, C. D.; Atkinson, K. R.; Baughman, R. H. Strong, Transparent, Multifunctional, Carbon Nanotube Sheets. *Science* **2005**, *309*, 1215–1219.
- Kim, J.; Ou, E.; Sellan, D. P.; Shi, L. A Four-Probe Thermal Transport Measurement for Nanostructures. *Rev. Sci. Instrum.* **2015**, *86*, 044901.
- Bergman, T. L.; Lavine, A. S.; Incropera, F. P.; DeWitt, D. P. *Fundamentals of Heat and Mass Transfer*, 7th ed.; Wiley, 2011; p 236.
- Tong, B.; Tan, Z. C.; Zhang, J. N.; Wang, S. X. Thermodynamic Investigation of Several Natural Polyols. *J. Therm. Anal. Calorim.* **2009**, *95*, 469–475.
- Zhichao, L.; Qiang, Z.; Gaohui, W. Preparation and Enhanced Heat Capacity of Nanotitania Doped Erythritol as Phase Change Material. *Int. J. Heat Mass Transfer* **2015**, *80*, 653–659.

34. Zalba, B.; Marin, J. M.; Cabeza, L. F.; Mehling, H. Review on Thermal Energy Storage with Phase Change: Materials, Heat Transfer Analysis and Applications. *Appl. Therm. Eng.* **2003**, *23*, 251–283.
35. Agyenima, F.; Eames, P.; Smyth, M. Experimental Study on the Melting and Solidification Behavior of a Medium Temperature Phase Change Storage Material (Erythritol) System Augmented with Fins to Power a LiBr/H₂O Absorption Cooling System. *Renewable Energy* **2011**, *36*, 108–117.
36. Alexiades, V.; Solomon, A. D.; Wilson, D. G. The Formation of a Solid Nucleus in Supercooled Liquid, I. *J. Non-Equilib. Thermodyn.* **1988**, *13*, 281–300.
37. Ona, E. P.; Zhang, X.; Kyaw, K.; Watanabe, F.; Matsuda, H.; Kakiuchi, H.; Yabe, M.; Chihara, S. Relaxation of Supercooling of Erythritol for Latent Heat Storage. *J. Chem. Eng. Jpn.* **2001**, *34*, 376–382.
38. Jankowski, N. R.; McCluksey, F. P. Electrical Supercooling Mitigation in Erythritol. In *Proceedings of the 14th International Heat Transfer Conference*, Vol. 7; Washington, DC, **2010** August 7–13, p 409.
39. Garcia-Romero, A.; Diarce, G.; Ibarretxe, J.; Urresti, A.; Sala, J. M. Influence of the Experimental Conditions on the Subcooling of Glauber's Salt When Used as PCM. *Sol. Energy Mater. Sol. Cells* **2012**, *102*, 189–195.
40. Diao, Y.; Harada, T.; Myerson, A. S.; Hatton, T. A.; Trout, B. L. The Role of Nanopore Shape in Surface-Induced Crystallization. *Nat. Mater.* **2011**, *10*, 867–871.
41. Asanithi, P. Surface Porosity and Roughness of Micrographite Film for Nucleation of Hydroxyapatite. *J. Biomed. Mater. Res., Part A* **2014**, *102*, 2590–2599.
42. Das, A.; Stöckelhuber, K. W.; Jurk, R.; Saphiannikova, M.; Fritzsche, J.; Lorenz, H.; Klüppel, M.; Heinrich, H. Modified and Unmodified Multiwalled Carbon Nanotubes in High Performance Solutionstyrene-Butadiene and Butadiene Rubber Blends. *Polymer* **2008**, *49*, 5276–5283.
43. Oya, T.; Nomura, T.; Okinaka, N.; Akiyama, T. Phase Change Composite Based on Porous Nickel and Erythritol. *Appl. Therm. Eng.* **2012**, *40*, 373–377.
44. Oya, T.; Nomura, T.; Tsubota, M.; Okinaka, N.; Akiyama, T. Thermal Conductivity Enhancement of Erythritol as PCM by Using Graphite and Nickel Particles. *Appl. Therm. Eng.* **2013**, *61*, 825–828.